Research Square

Preprints are preliminary reports that have not undergone peer review.
They should not be considered conclusive, used to inform clinical practice,
or referenced by the media as validated information.

A ZIF-8 Derived Nano-Porous Carbon as Solid Transducing Layer in High-Performance All-Solid-State Sodium Ion Selective Electrodes

Peike Wang
Harbin Institute of Technology (Shenzhen)
Shuheng Fan
fanshuhengheng@163.com
Harbin Institute of Technology (Shenzhen)
Haipeng Liu
Harbin Institute of Technology (Shenzhen)
Shiqiang Zhou
Harbin Institute of Technology (Shenzhen)
Jingjing Luo
Harbin Institute of Technology (Shenzhen)
Yuan Meng
Harbin Institute of Technology (Shenzhen)
Jin Ning
Harbin Institute of Technology (Shenzhen)
Suzhu Yu
Harbin Institute of Technology (Shenzhen)
Jun Wei
Harbin Institute of Technology (Shenzhen)

Research Article

Keywords: solid transducing layer, nanoporous-carbon, double-layer capacitance, hydrophobicity

Posted Date: April 30th, 2026

DOI: https://doi.org/10.21203/rs.3.rs-9279543/v1

License: This work is licensed under a Creative Commons Attribution 4.0 International License.
Read Full License

Additional Declarations: No competing interests reported.

Abstract

Graphene and carbon nanotubes, common solid transducing materials for solid-contact ion-selective electrodes (SC-ISEs), face limitations due to their intrinsic microstructures, which motivates the development of alternative carbon-based materials to address these performance bottlenecks. Herein, we report the synthesis of hydrophobic nanoporous-carbon (NPC) using a zeolitic imidazolate framework-8 (ZIF-8) template under a mixed nitrogen-hydrogen atmosphere. This integrated design strategy simultaneously achieves high specific surface area, nitrogen-doped double-layer capacitance, and superior hydrophobicity by minimizing polar oxygen-containing functional groups. These combined attributes effectively enhance sensitivity and long-term stability by suppressing aqueous layer formation at the interface. For Na^+ sensing, the resulting SC-ISEs exhibited a Super-Nernstian sensitivity of 64.11 $mV \cdot dec^{-1}$ and a detection limit of $10^{-4.7}$ M, demonstrating that the innovative application of ZIF-8-derived hydrophobic NPC provides a superior pathway for developing high-performance SC-ISEs that outperform most reported solid transducing materials.

Introduction

Ion-selective electrodes (ISEs) are widely applied in various fields, including environmental monitoring and disease diagnosis[1]. The development of miniaturized, calibration-free, low-cost, and high-precision ISEs for real-time in situ monitoring has become an important research direction[2]. Compared with liquid-contact ISEs (LC-ISEs), solid-contact ISEs (SC-ISEs) exhibit higher sensitivity, lower detection limits, and better biocompatibility[3]. A typical SC-ISE consists of an ion-selective membrane (ISM), a solid transducing layer (STL), and a supporting electrode[4]. The STL serves as the ion-to-electron transducer between the ISM and SE, converting the ionic signal into an electronic one. Rational design of the composition and structure of the STL is therefore critical to further improving the performance of SC-ISEs. An ideal STL should possess high capacitance and excellent hydrophobicity[5]. Solid transducing materials can be classified into two categories: double-layer capacitive materials and pseudocapacitive materials[6]. Double-layer capacitive materials generally exhibit better stability than pseudocapacitive materials[7].

Carbon-based materials, as typical double-layer capacitive materials, have attracted extensive attention owing to their tunable composition and structure, which enable adjustable solid transducing performance[8]. Carbon nanotubes (CNTs)[9–11], graphene[12] and carbon black (CB)[13, 14] are the three most commonly used carbon-based materials in SC-ISEs. Although these materials have enabled SC-ISEs to achieve near-Nernstian responses and improved potential stability[15–17], their performance remains constrained by inherent microstructural limitations, which hinder further enhancement of their capacitive properties. To overcome these microstructural constraints, nanoporous-carbon (NPC) have emerged as a promising alternative, offering greater flexibility in the regulation of composition and morphological characteristics[18, 19].

Organic framework-derived NPC generally exhibit ultrahigh double-layer capacitance, which is favorable for improving the sensitivity of SC-ISEs[20, 21]. However, many such materials suffer from poor hydrophobicity, leading to the formation of an undesirable water layer and insufficient long-term stability. While some progress has been made—for instance, the Bühlmann group utilized three-dimensionally ordered microporous carbon to achieve an ultralow potential drift of 11.7 $mV \cdot h^{-1}$ [22]—developing NPC that simultaneously possess high capacitance and robust hydrophobicity remains a significant challenge. Zeolitic imidazolate framework-8 (ZIF-8), a typical metal-organic framework (MOF), is an ideal precursor for synthesizing such materials due to its uniform pore size, high nitrogen content, and ease of carbonization, resulting in carbon structures with abundant nanopores[23, 24]. Despite these advantages, the application of ZIF-8-derived NPC as the STL in SC-ISEs remains largely unexplored.

In this work, we employ ZIF-8 templates to synthesize NPC via pyrolysis under a mixed nitrogen-hydrogen atmosphere. The as-prepared NPC inherits the high specific surface area of the ZIF-8 template, providing high double-layer capacitance. Furthermore, the introduction of hydrogen during synthesis inhibits the formation of polar oxygen-containing functional groups on the surface, endowing the material with excellent hydrophobicity. Sodium-ion SC-ISEs using the as-prepared NPC as the STL exhibit Nernstian sensitivity, low detection limits, and excellent long-term stability, outperforming most previously reported counterparts.

Experimental segment

Chemicals

The synthetic raw materials zinc nitrate, ammonium chloride, potassium ferricyanide, isopropyl alcohol, tetrahydrofuran, 2-methylimidazole, sodium chloride, potassium chloride, sodium tetrakis [3,5-bis(trifluoromethyl) phenyl] borate, bis(2-ethylhexyl)sebacate, poly(vinyl chloride) and sodium ionophore x were obtained from Beijing Innochem Science & Technology Co., Ltd. Commercial materials graphene and multi-walled carbon nanotubes (MWCNTs) were obtained from Jiangsu Xianfeng Nano Material Technology Co., Ltd. All materials were obtained from commercial sources and used without further treatment.

Synthesis of ZIF-8

Methanol solutions of zinc nitrate (0.094 $mol \cdot L^{-1}$) and 2-methylimidazole (0.375 $mol \cdot L^{-1}$) were prepared separately. Subsequently, the zinc nitrate solution was added to the 2-methylimidazole solution under stirring at a volume ratio of 1:1. The mixed solution was left to stand at room temperature for 24 h. After thorough washing with deionized water and ethanol, ZIF-8 was collected via centrifugation. The product was dried under vacuum at 60°C for 24 h to remove residual solvents.

Synthesis of ZIF-8 derived nano-porous carbon

ZIF-8 was pyrolyzed under a N_2/H_2 flow (90%/10% volume ratio) at 950°C for 2 h, with a heating rate of 5°C·min^{-1}. The resulting product was denoted as NPC.

Preparation of SC-ISEs

Solid transducing layer

Solid transducing layer ink was prepared by dispersing solid transducing materials (2 mg) in the mixed solution of deionized water (800 μL), isopropanol (200 μL) and 5 wt.% Nafion (40 μL). After sonicated for 30 min, the ink (60 μL) was cast onto the glassy carbon electrode with a diameter of 6 mm to form the solid transducing layer.

Na^+ selective membrane

The Na^+ selective membrane cocktail solution was prepared by dispersing 65.45 wt.% sebacic acid (261.8 mg), 0.55 wt.% sodium borate (2.2 mg), 33 wt.% polyvinyl chloride (132 mg) and 1 wt.% tetraethyl tetraacetate (4 mg) in tetrahydrofuran (2640 μL). The cocktail solution (20 μL) was cast onto the solid transducing layers to form the ion selective membrane.

Characterization

Scanning electron microscopy (SEM) images were obtained by a Hitachi S-4800 with electron acceleration energy of 5 kV. Transmission electron microscopy (TEM) images were collected on a JEOL JEM-2100F with electron acceleration energy of 200 kV. The crystal structure of the catalysts was examined by a DX-2700BH with Cu K_α radiation (λ = 1.5406 Å) with a step size of 0.2°. Specific surface area was measured based on Brunauer-Emmett-Teller method using AutosorbiQ instrument (Quantachrome) at liquid nitrogen temperature. Detailed chemical compositions were analyzed by X-ray photoelectron spectroscopy (XPS) on an Axis Supra instrument from Kratos Analytical Ltd. using a monochromatic Al K_α X-ray beam (1,486.6 eV). A Shirley background was applied to all spectra. All the spectra were charge referenced to 284.8 eV. Raman spectra were performed in backscattering mode on a Thermo Fisher Raman microscope using a 532 nm laser. Fourier transform infrared spectroscopy (FTIR) were measured on a Thermo Fisher IS10 infrared spectrometer.

Capacitive and SC-ISEs performance analysis

All the electrochemical tests including cyclic voltammetry (CV) and galvanostatic charge-discharge (GCD) measurements were conducted on CHI 760E workstations in a typical three-electrode system. A double salt bridge Ag/AgCl was used as the reference and a Pt foil was used as the counter electrode.

The electrochemical active surface areas (ECSA) were calculated using the Randles–Ševčík equation:

$$i_p = (2.69 \times 10^5) n^{3/2} A C D^{1/2} v^{1/2}$$

1

Where i_p is the peak current obtained by cyclic voltammetry in ferrocyanide solution, *n* is the number of electrons transferred during redox, *A* is the ECSA, *C* is the concentration, *D* is the diffusion coefficient and *v* is the scan rate.

Results and discussion

Materials characterization

To establish a foundation for subsequent performance evaluations, a comprehensive suite of characterization techniques was employed to verify the morphology and microstructure of the synthesized NPC. SEM and TEM were utilized to observe the material's morphology. As depicted in Fig.s1b and 1c, the NPC retains a rhombic dodecahedron shape with an average particle size of 113.7 nm, aligning with previously reported ZIF-8 templates[25].

High-resolution TEM (HRTEM) and X-ray diffraction (XRD) provided insights into the crystal structure. The HRTEM image (Fig. 1d.) reveals the amorphous nature of the NPC, a finding further corroborated by the XRD pattern in Fig. 1e. For structural comparison with traditional carbon materials, the XRD patterns of control graphene and MWCNT samples are provided in Fig. S2. Raman spectroscopy was further employed to analyze the carbon framework. As shown in Fig. 1f, the Raman spectrum of the NPC is characterized by three prominent bands: the D band (disordered carbon, ~ 1300–1400 cm^{-1}), the G band (graphitic carbon, ~ 1580 cm^{-1}), and the 2D band (~ 2680 cm^{-1})[26]. The calculated ID/IG ratio of 0.92 indicates a high degree of structural disorder and defects within the carbon skeleton, which is consistent with the amorphous nature observed via HRTEM and XRD[27, 28]. Raman spectra of graphene and MWCNT controls (Fig. S3) serve as structural benchmarks and align with literature values.

To investigate the porosity, N_2 adsorption-desorption measurements were conducted. The isotherm (Fig. 1g) displays characteristic features of nanoporous materials[29, 30], including a sharp nitrogen uptake at low relative pressures ($P/P_0 < 0.05$) and a gradual increase between $P/P_0 = 0.2$ and 0.9, signifying the presence of abundant micropores. This is further confirmed by the pore size distribution curve (Fig. S4), which shows that the pores are primarily concentrated within the 0–3 nm range. In summary, the synthesized NPC possesses a high specific surface area and a rich microporous architecture. These structural attributes are highly advantageous for its application as a solid transducer layer, providing a robust platform for the subsequent electrochemical performance discussions.

To elucidate the chemical origins of the material's hydrophobicity, XPS and FTIR were performed. The high-resolution C 1s XPS spectrum (Fig. 2a) reveals peaks corresponding to C–C (284.8 eV)[31, 32], C–N (286.25 eV)[18], C–O (288.14 eV)[33], and C = O (290.22 eV)[33]. Nitrogen species are further identified in the N 1s spectrum (Fig. 2b) as pyridinic N (398.50 eV), pyrrolic N (400.66 eV), and graphitic N (401.96

eV), while the O 1s spectrum confirms the presence of C–O (532.02 eV) and C = O (533.79 eV) bonds. These results, compared alongside the control graphene and MWCNT samples (Fig. S5)[34, 35], highlight the specific surface chemistry of the NPC.

FTIR characterization provides further evidence: the spectrum of NPC exhibits C–H out-of-plane bending (672 cm^{-1})[36], C–O stretching (1150–1300 cm^{-1})[37, 38], and C = O stretching (1588 cm^{-1})[36]. Notably, the hydroxyl (–OH) stretching vibration peak at 1734 cm^{-1} [39] is completely absent, which contrasts sharply with the control graphene and MWCNT samples where –OH groups are clearly observed (Fig. S6). This lack of hydrophilic functional groups (Table S1) directly contributes to the superior hydrophobicity of NPC[40].

In water contact angle measurements, NPC achieves a value of 157.7°, outperforming both graphene (154.7°) and MWCNTs (151.4°). This chemical state and the resulting exceptional hydrophobicity are critical for suppressing the formation of an interfacial water layer at the ISM/STL interface, thereby ensuring the long-term potential stability of SC-ISEs.

Capacitive performance analysis

To establish the potential of NPC as a high-performance solid transduction layer, its capacitive performance was systematically evaluated and compared with graphene and MWCNTs in a 0.1 M NaCl solution. CV measurements revealed quasi-rectangular shapes for all samples (Fig. 3a, Fig. S7a–S7c), characteristic of typical double-layer capacitance. Notably, NPC exhibited the largest integrated area, signifying a superior double-layer capacitance compared to the other materials[41].

GCD profiles (Fig. 3b, Fig. S7d–S7f) further confirmed this behavior through their linear and symmetric shapes, indicating excellent electrochemical reversibility and high coulombic efficiency[42]. Calculations derived from these curves yielded a specific capacitance of 163 $F \cdot g^{-1}$ for NPC, remarkably exceeding that of graphene (15.63 $F \cdot g^{-1}$) and MWCNT (7.52 $F \cdot g^{-1}$).

ECSA was assessed using a ferricyanide redox probe. Consistent with the Randles-Sevcik model (Fig. 3c)[43], all samples exhibited reversible redox characteristics. According to the Randles-Sevcik equation (Eq. 1, Supporting Information), ECSA is proportional to the peak current. NPC displayed the highest peak current (353.9 μA) relative to graphene (300.9 μA) and MWCNT (162.6 μA), confirming it possesses the most extensive ECSA.

To further elucidate charge transfer kinetics, electrochemical impedance spectroscopy (EIS) was employed. Nyquist plots (Fig. 3d) demonstrate that NPC exhibits the smallest semicircle diameter and the steepest low-frequency slope, representing the lowest charge transfer resistance and ion diffusion resistance among the tested materials[42]. These results demonstrate that NPC provides a large ECSA and abundant adsorption sites for electrolyte ions, facilitating significantly enhanced double-layer capacitance.

This superior electrochemical performance is highly consistent with the unique nanoporous architecture and favorable chemical properties established in the preceding characterization section. Importantly, the combination of high capacitance, large ECSA, and minimized resistance fulfills the critical requirements for an ideal STL, providing a robust theoretical foundation for the subsequent evaluation of its performance in SC-ISEs[44].

SC-ISEs performance analysis

The assembly structure of the sodium-ion SC-ISEs is illustrated in Fig. 4a. A typical sodium-ion SC-ISE consists of a glassy carbon electrode (GCE), an STL, and a Na^+-selective ISM. The open-circuit potential (OCP) response and corresponding calibration curves for SC-ISEs using bare GCE, NPC, MWCNT, and graphene as the STL were measured in a series of NaCl solutions to evaluate electrode sensitivity. The NPC and graphene-based SC-ISEs demonstrated an extended continuous response range from 10^{-6} to 10^{-1} M, whereas the MWCNT-based electrode and the bare GCE were restricted to ranges of 10^{-5}–10^{-1} M and 10^{-3}–10^{-1} M, respectively (Fig. 4b). This broader response range for NPC and graphene directly demonstrates their advantages as STLs, which is attributed to their higher capacitance and larger electrochemical active surface area. As summarized in Fig. 4c and Table S2, the NPC-based SC-ISE demonstrated a superior sensitivity of 64.11 mV·dec^{-1} and a detection limit of $10^{-4.7}$ M, outperforming the graphene-based (61.21 mV·dec^{-1}; $10^{-4.8}$ M), MWCNT-based (59.85 mV·dec^{-1}; $10^{-4.5}$ M), and bare GCE (42.9 mV·dec^{-1}; $10^{-2.3}$ M) electrodes. This super-Nernstian response of the NPC electrode indicates its optimal performance, which is intrinsically linked to its high capacitance.

Aqueous layer formation tests were performed by alternately exposing the SC-ISEs to primary ion (Na^+) and interfering ion (NH_4^+) solutions for 1 h each. Although all SC-ISEs exhibited relatively stable potential responses in both NaCl and NH_4Cl solutions (Fig. 4d), the NPC-based electrode demonstrated the most robust stability. While the hydrophobicity of the STLs generally helps prevent water layer formation, the superior stability of the NPC electrode is specifically driven by the synergy between its excellent hydrophobicity and high capacitance. Chronopotentiometry at ± 1 nA cm^{-2} was further performed to evaluate the short-term potential stability of the SC-ISEs. As shown in Fig. 4e, the NPC-based system exhibited the smallest potential fluctuations, confirming that its unique structural properties effectively stabilize the phase boundary and minimize potential drift.

Figure 5 schematically illustrates the Na^+ transduction mechanism of the NPC-based SC-ISEs. Initially, Na^+ in the solution complexes with the ionophore L within the ISM to form Na^+-L complexes. Specifically, the high specific surface area and abundant porous structure of the NPC provide a multitude of active sites for the formation of an electric double layer between the electrons in the STL and the Na^+-L complexes. This high-capacitance characteristic of the NPC ensures a stable and efficient charge transfer at the electrode interface, thereby establishing an interfacial potential. This interfacial potential is measured to determine the Na^+ activity in the solution.

Conclusions

The integration of high-surface-area ZIF-8 derivatives with controlled atmospheric pyrolysis yields a superior nanoporous-carbon (NPC)-based STL for SC-ISEs. The high double-layer capacitance of this NPC is derived from its substantial specific surface area and nitrogen-doped structural motifs. Crucially, pyrolysis under a mixed nitrogen-hydrogen atmosphere significantly enhances material hydrophobicity, thereby mitigating the formation of detrimental aqueous layers and bolstering electrode stability. Synergizing high double-layer capacitance with excellent hydrophobicity allows the Na^+-selective SC-ISEs to achieve a superior sensitivity of 64.11 $mV \cdot dec^{-1}$, a low detection limit of $10^{-4.7}$ M, and exceptional potential stability. These performance metrics surpass most reported STL materials, marking a significant advancement in electrochemical ion sensing. By demonstrating a rational design strategy for optimizing carbon materials, this work provides a robust methodology for developing advanced carbon-based architectures for diverse electrochemical applications beyond SC-ISEs. Future research could extend this strategy to the fabrication of multi-ion sensing platforms or further refine the pore structure of ZIF-derived carbons to achieve even lower detection limits in complex biological matrices.

Declarations

Supplementary Information The online version contains supplementary material available at

Acknowledgments This work was financially supported by Shenzhen Science and Technology Innovation Program (Grant No. KQTD20200820113045083, ZDSYS20190902093220279, JCYJ20220818102403007), Shenzhen Research Fund for Returned Scholars (DD4500100125, DD2440800624)

Author contributions Peike Wang: Conceptualization, Methodology, Investigation, Writing – original draft. Shuheng Fan: Formal analysis, Investigation, Writing – original draft. Haipeng Liu: Formal analysis, Investigation. Shiqiang Zhou: Investigation. Jingjing Luo: Investigation. Yuan Meng: Investigation. Jin Ning: Investigation. Suzhu Yu: Conceptualization, Formal analysis, Writing – review & editing, Supervision; Jun Wei: Conceptualization, Writing – review & editing, Supervision, Project Administration, Funding Acquisition.

Data availability Data will be made available on request.

Conflict of interest The authors declare that they have no known competing financial interests or personal relationships that could have appeared to influence the work reported in this paper.

References

1. Wardak C, Morawska K, Pietrzak K (2023) New Materials Used for the Development of Anion-Selective Electrodes-A Review. https://doi.org/10.3390/ma16175779. MATERIALS 16

2. Shao YZ, Ying YB, Ping JF (2020) Recent advances in solid-contact ion-selective electrodes: functional materials, transduction mechanisms, and development trends. Chem Soc Rev 49:4405–4465. https://doi.org/10.1039/c9cs00587k
3. Ding JW, Qin W (2020) Recent advances in potentiometric biosensors. TRAC-TRENDS IN ANALYTICAL CHEMISTRY 124. https://doi.org/10.1016/j.trac.2019.115803
4. Parrilla M, Cuartero M, Crespo GA (2019) Wearable potentiometric ion sensors. TRAC-TRENDS Anal Chem 110:303–320. https://doi.org/10.1016/j.trac.2018.11.024
5. Paczosa-Bator B, Cabaj L, Pięk M et al (2015) Carbon-Supported Platinum Nanoparticle Solid-State Ion Selective Electrodes for the Determination of Potassium. Anal Lett 48:2773–2785. https://doi.org/10.1080/00032719.2015.1045594
6. Jiang T, Yin B, Liu X et al (2022) Porous carbon-based robust, durable, and flexible electrochemical device for K+ detection in sweat†. Analyst 147:1144–1151. https://doi.org/10.1039/d1an02322e
7. Neal JN, Wesolowski DJ, Henderson D et al (2017) Ion distribution and selectivity of ionic liquids in microporous electrodes. J Chem Phys 146:174701. https://doi.org/10.1063/1.5009923
8. Wang PK, Liu HP, Zhou SQ et al (2023) A Review of the Carbon-Based Solid Transducing Layer for Ion-Selective Electrodes. https://doi.org/10.3390/molecules28145503. MOLECULES 28
9. Mousavi Z, Teter A, Lewenstam A et al (2011) Comparison of Multi-walled Carbon Nanotubes and Poly (3-octylthiophene) as Ion-to-Electron Transducers in All-Solid-State Potassium Ion-Selective Electrodes. Electroanal 23:1352–1358. https://doi.org/10.1002/elan.201000747
10. Guinovart T, Parrilla M, Crespo GA et al (2013) Potentiometric sensors using cotton yarns, carbon nanotubes and polymeric membranes. Analyst 138:5208–5215. https://doi.org/10.1039/c3an00710c
11. Crespo GA, Macho S, Rius FX (2008) Ion-selective electrodes using carbon nanotubes as ion-to-electron transducers. Anal Chem 80:1316–1322. https://doi.org/10.1021/ac071156l
12. Li F, Ye J, Zhou M et al (2012) All-solid-state potassium-selective electrode using graphene as the solid contact. Analyst 137:618–623. https://doi.org/10.1039/c1an15705a
13. Mazzaracchio V, Serani A, Fiore L et al (2021) All-solid state ion-selective carbon black-modified printed electrode for sodium detection in sweat. Electrochim Acta 394. https://doi.org/10.1016/j.electacta.2021.139050
14. Paczosa-Bator B, Cabaj L, Piech R et al (2013) Potentiometric sensors with carbon black supporting platinum nanoparticles. Anal Chem 85:10255–10261. https://doi.org/10.1021/ac402885y
15. Appiah-Ntiamoah R, Gadisa BT, Kim H (2018) An effective electrochemical sensing platform for fluoride ions based on fluorescein isothiocyanate-MWCNT composite. New J Chem 42:11341–11350. https://doi.org/10.1039/c8nj01703d
16. An Q, Gan S, Xu J et al (2019) A multichannel electrochemical all-solid-state wearable potentiometric sensor for real-time sweat ion monitoring. Electrochem Commun 107. https://doi.org/10.1016/j.elecom.2019.106553

17. Ozer T, Henry CS (2022) Microfluidic-based ion-selective thermoplastic electrode array for point-of-care detection of potassium and sodium ions. Microchim Acta 189. https://doi.org/10.1007/s00604-022-05264-y
18. Salunkhe RR, Kamachi Y, Torad NL et al (2014) Fabrication of symmetric supercapacitors based on MOF-derived nanoporous carbons. J Mater Chem A 2:19848–19854. https://doi.org/10.1039/c4ta04277h
19. Salunkhe RR, Tang J, Kamachi Y et al (2015) Asymmetric Supercapacitors Using 3D Nanoporous Carbon and Cobalt Oxide Electrodes Synthesized from a Single Metal-Organic Framework. ACS Nano 9:6288–6296. https://doi.org/10.1021/acsnano.5b01790
20. Mun WJ, Kim B, Moon SJ et al (2024) Hydrogen-bonded organic framework-derived, flower-on-fiber-like, carbon nanofiber electrodes for supercapacitors. J Mater Chem A 12:6712–6723. https://doi.org/10.1039/d3ta06722j
21. Yin J, Zhang W, Alhebshi NA et al (2020) Synthesis strategies of porous carbon for supercapacitor applications. Small methods 4:1900853. https://doi.org/10.1002/smtd.201900853
22. Lai C-Z, Fierke MA, Stein A et al (2007) Ion-selective electrodes with three-dimensionally ordered macroporous carbon as the solid contact. Anal Chem 79:4621–4626. https://doi.org/10.1021/ac070132b
23. Yang WP, Li XX, Li Y et al (2019) Applications of Metal-Organic-Framework-Derived Carbon Materials. https://doi.org/10.1002/adma.201804740. ADVANCED MATERIALS 31
24. Wan L, Shamsaei E, Easton CD et al (2017) ZIF-8 derived nitrogen-doped porous carbon/carbon nanotube composite for high-performance supercapacitor. Carbon 121:330–336. https://doi.org/10.1016/j.carbon.2017.06.017
25. Huang HJ, Qin JL, Liu C et al (2024) Constructing Zn-based MOF-MXene nanoarchitectures to stabilize ultrafine Pt nanocrystals with enhanced methanol oxidation performance. https://doi.org/10.1016/j.carbon.2024.119171. CARBON 226
26. Ferrari AC, Basko DM (2013) Raman spectroscopy as a versatile tool for studying the properties of graphene. Nat Nanotechnol 8:235–246. https://doi.org/10.1038/nnano.2013.46
27. Li Z, Deng L, Kinloch IA et al (2023) Raman spectroscopy of carbon materials and their composites: Graphene, nanotubes and fibres. Prog Mater Sci 135:101089. https://doi.org/10.1016/j.pmatsci.2023.101089
28. Zhang P, Fan J, Wang Y et al (2024) Insights into the role of defects on the Raman spectroscopy of carbon nanotube and biomass-derived carbon. Carbon 222:118998. https://doi.org/10.1016/j.carbon.2024.118998
29. Baldovino-Medrano VCG, Niño-Celis V, Isaacs Giraldo R (2023) Systematic analysis of the nitrogen adsorption–desorption isotherms recorded for a series of materials based on microporous–mesoporous amorphous aluminosilicates using classical methods. J Chem Eng Data 68:2512–2528. https://doi.org/10.1021/acs.jced.3c00257

30. Ravikovitch PI, Neimark AV (2001) Characterization of nanoporous materials from adsorption and desorption isotherms. Colloids Surf A 187:11–21. https://doi.org/10.1016/S0927-7757(01)00614-8
31. Qu YT, Li ZJ, Chen WX et al (2018) Direct transformation of bulk copper into copper single sites via emitting and trapping of atoms. Nat Catal 1:781–786. https://doi.org/10.1038/s41929-018-0146-x
32. Ganguly A, Sharma S, Papakonstantinou P et al (2011) Probing the Thermal Deoxygenation of Graphene Oxide Using High-Resolution In Situ X-ray-Based Spectroscopies. J Phys Chem C 115:17009–17019. https://doi.org/10.1021/jp203741y
33. Liu HP, Zhu SL, Cui ZD et al (2021) Boosting oxygen reduction catalysis with abundant single atom tin active sites in zinc-air battery. J Power Sources 490. https://doi.org/10.1016/j.jpowsour.2021.229483
34. Chiang Y-C, Lee C-Y, Lee H-C (2007) Surface chemistry of polyacrylonitrile-and rayon-based activated carbon fibers after post-heat treatment. Mater Chem Phys 101:199–210. https://doi.org/10.1016/j.matchemphys.2006.03.007
35. Tang Q, Li B, Ma W et al (2020) Fabrication of a double-layer membrane cathode based on modified carbon nanotubes for the sequential electro-Fenton oxidation of p-nitrophenol. Environ Sci Pollut Res 27:18773–18783. https://doi.org/10.1007/s11356-020-08364-5
36. Raj AM, Thomas GC (2018) Tailoring of low grade coal to fluorescent nanocarbon structures and their potential as a glucose sensor. Sci Rep 8:13891. https://doi.org/10.1038/s41598-018-32371-9
37. Liu Y, Liu X, Dong W et al (2017) Efficient adsorption of sulfamethazine onto modified activated carbon: a plausible adsorption mechanism. Sci Rep 7:12437. https://doi.org/10.1038/s41598-017-12805-6
38. Li X, Hu Y, She D et al (2020) Modified activated carbon fiber felt for the electrosorption of norfloxacin in aqueous solution. Sustainability 12:3986. https://doi.org/10.3390/su12103986
39. Liu J, Liu Y, Peng J et al (2018) Preparation of high surface area oxidized activated carbon from peanut shell and application for the removal of organic pollutants and heavy metal ions. Water Air Soil Pollut 229:1–17. https://doi.org/10.1007/s11270-018-4021-9
40. Zhao G, Li J, Huang Y et al (2017) Robust Ni/WC superhydrophobic surfaces by electrodeposition. RSC Adv 7:44896–44903. https://doi.org/` 10.1039/c7ra08535d
41. Deng X, Li J, Zhu S et al (2019) Boosting the capacitive storage performance of MOF-derived carbon frameworks via structural modulation for supercapacitors. Energy Storage Mater 23:491–498. https://doi.org/10.1016/j.ensm.2019.04.015
42. Zhang M, Zhao N, Sha J et al (2014) Synthesis of novel carbon nano-chains and their application as supercapacitors. J Mater Chem A 2:16268–16275. https://doi.org/10.1039/c4ta02623c
43. Yeung KK, Li JW, Huang T et al (2022) Utilizing Gradient Porous Graphene Substrate as the Solid-Contact Layer To Enhance Wearable Electrochemical Sweat Sensor Sensitivity. https://doi.org/10.1021/acs.nanolett.2c01969. NANO LETTERS
44. Wang L, Wang C, Wang H et al (2018) ZIF-8 nanocrystals derived N-doped carbon decorated graphene sheets for symmetric supercapacitors. Electrochim Acta 289:494–502

https://doi.org/10.1016/j.electacta.2018.09.091

Figures

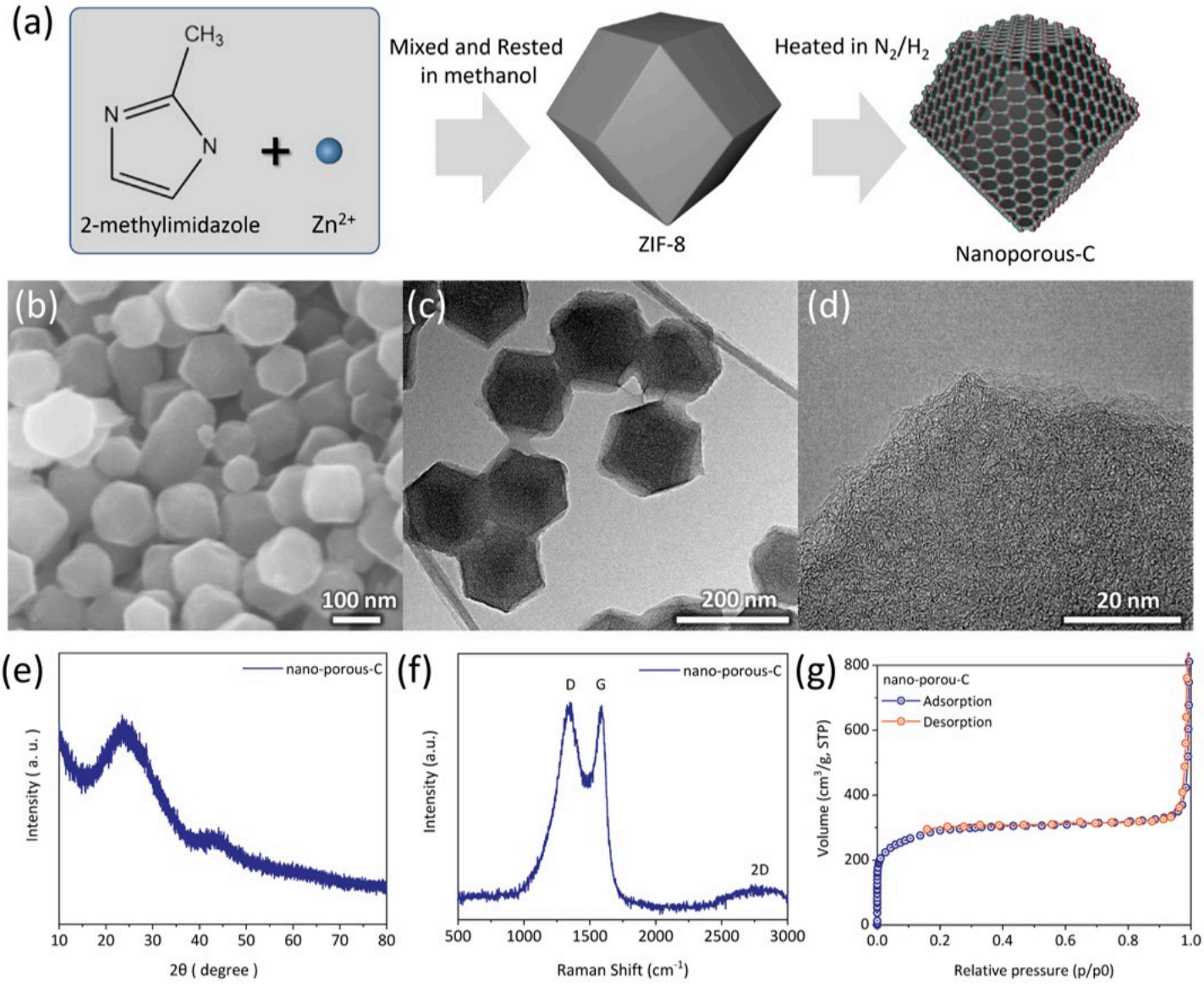


Figure 1

(a) Synthetic scheme of NPC. **(b)** SEM image, **(c)** TEM image, **(d)** HRTEM image, **(e)** XRD pattern, **(f)** Raman spectrum, and **(g)** N_2 adsorption-desorption isotherm of NPC

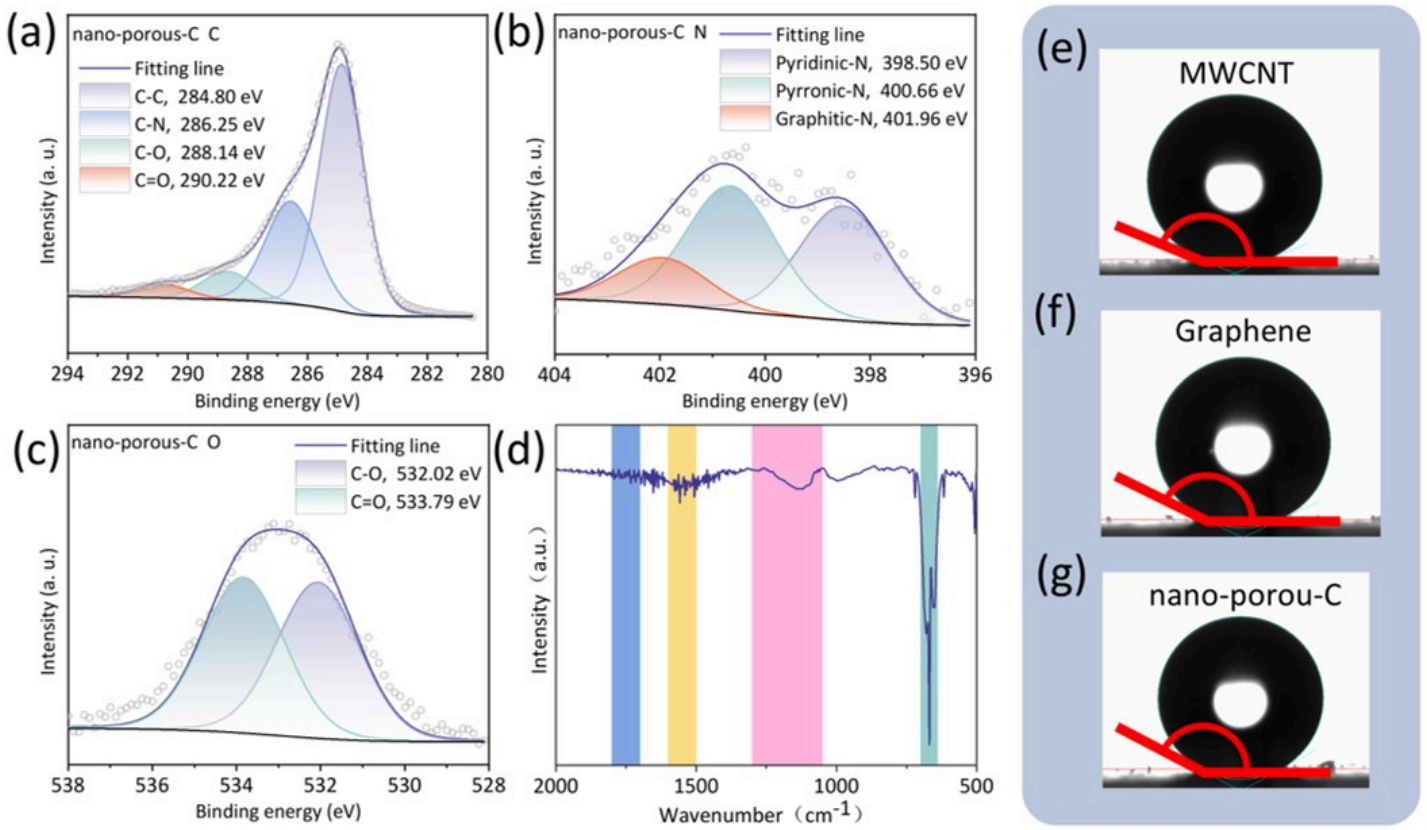


Figure 2

(a) C 1s, **(b)** N 1s, and **(c)** O 1s XPS spectra of the NPC. **(d)** FTIR spectrum of NPC. Water contact angle images of **(e)** MWCNT, **(f)** graphene, and **(g)** NPC

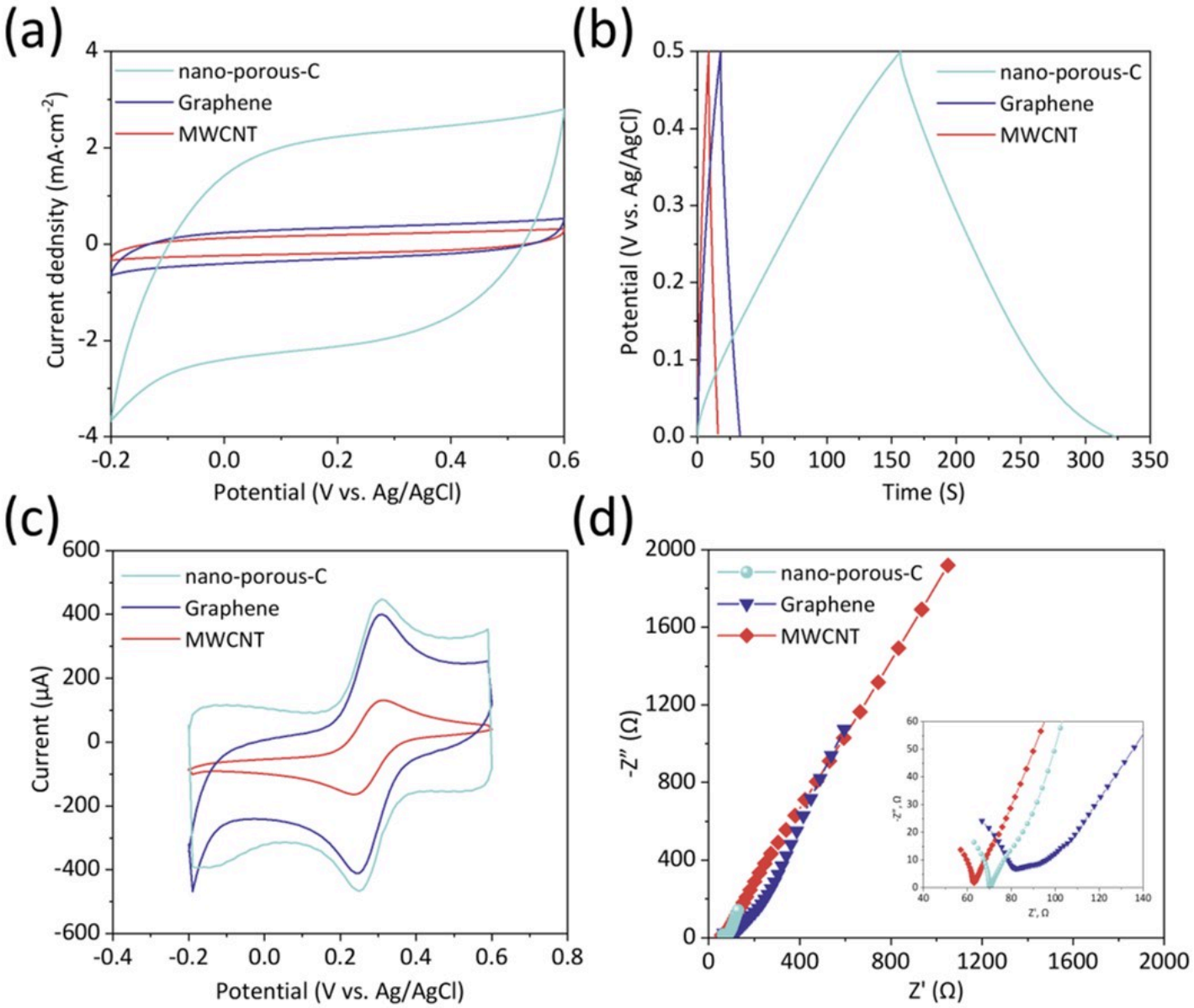


Figure 3

Capacitive performance evaluation of NPC, graphene and MWCNT. **(a)** CV curves tested in a 0.1 M NaCl solution at 50 $mV \cdot s^{-1}$. **(b)** GCD curves at 0.5 $A \cdot g^{-1}$. **(c)** CV curves in a 10 mM ferricyanide and 1 M NaCl solution at 30 $mV \cdot s^{-1}$. **(d)** Nyquist plots at open-circuit potential in a 0.1 M NaCl solution; inset is the enlargement at the high-frequency region

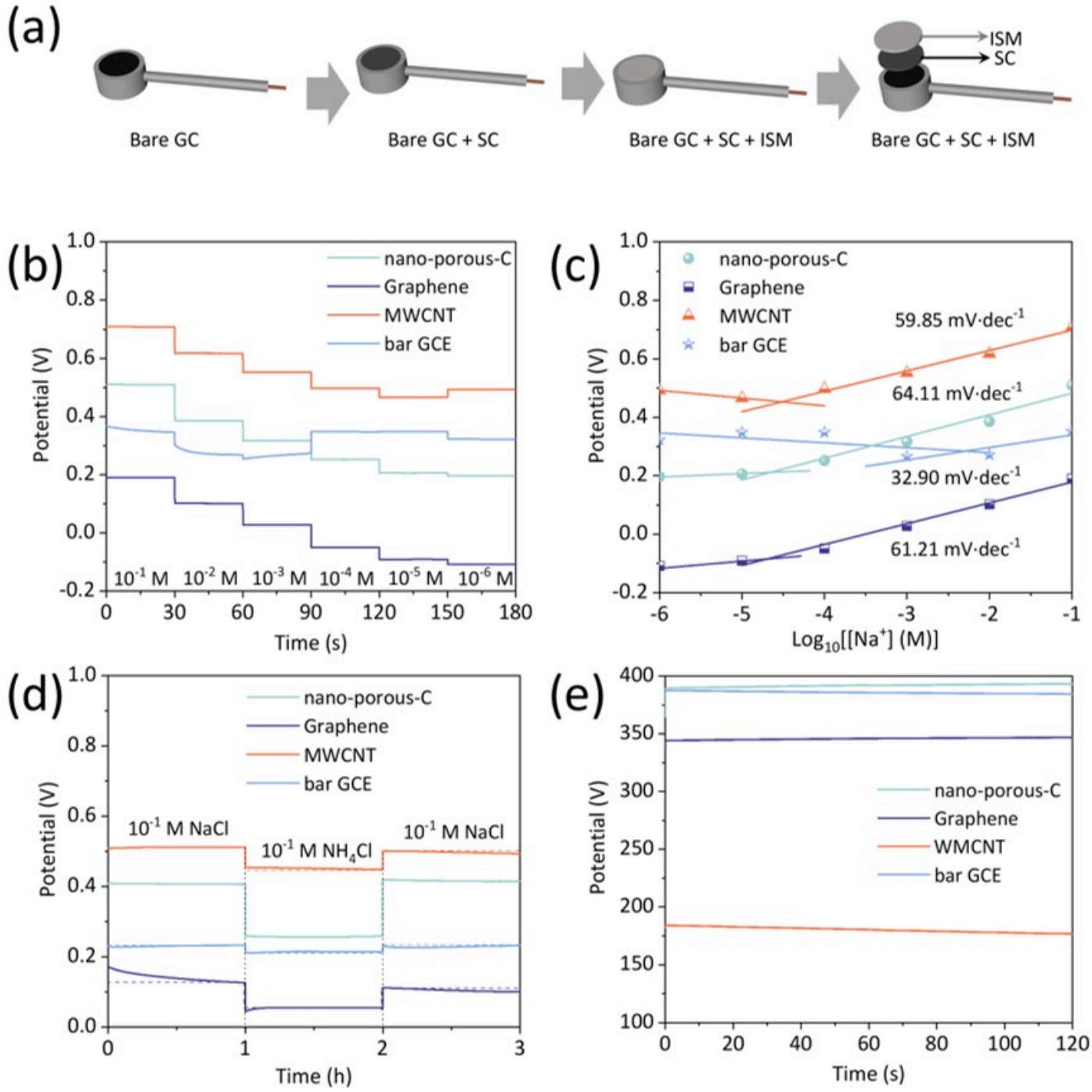


Figure 4

Electrochemical measurements of SC-ISEs using bare glass carbon electrode, NPC, MWCNT, and graphene as solid transducing layers. **(a)** Schematic of the SC-ISE fabrication process, **(b)** OCP response plots in a series of NaCl solutions, **(c)** response calibration curves, **(d)** water layer test results, **(e)** chronopotentiograms under a constant current of ±1 nA in 1 mM NaCl solution

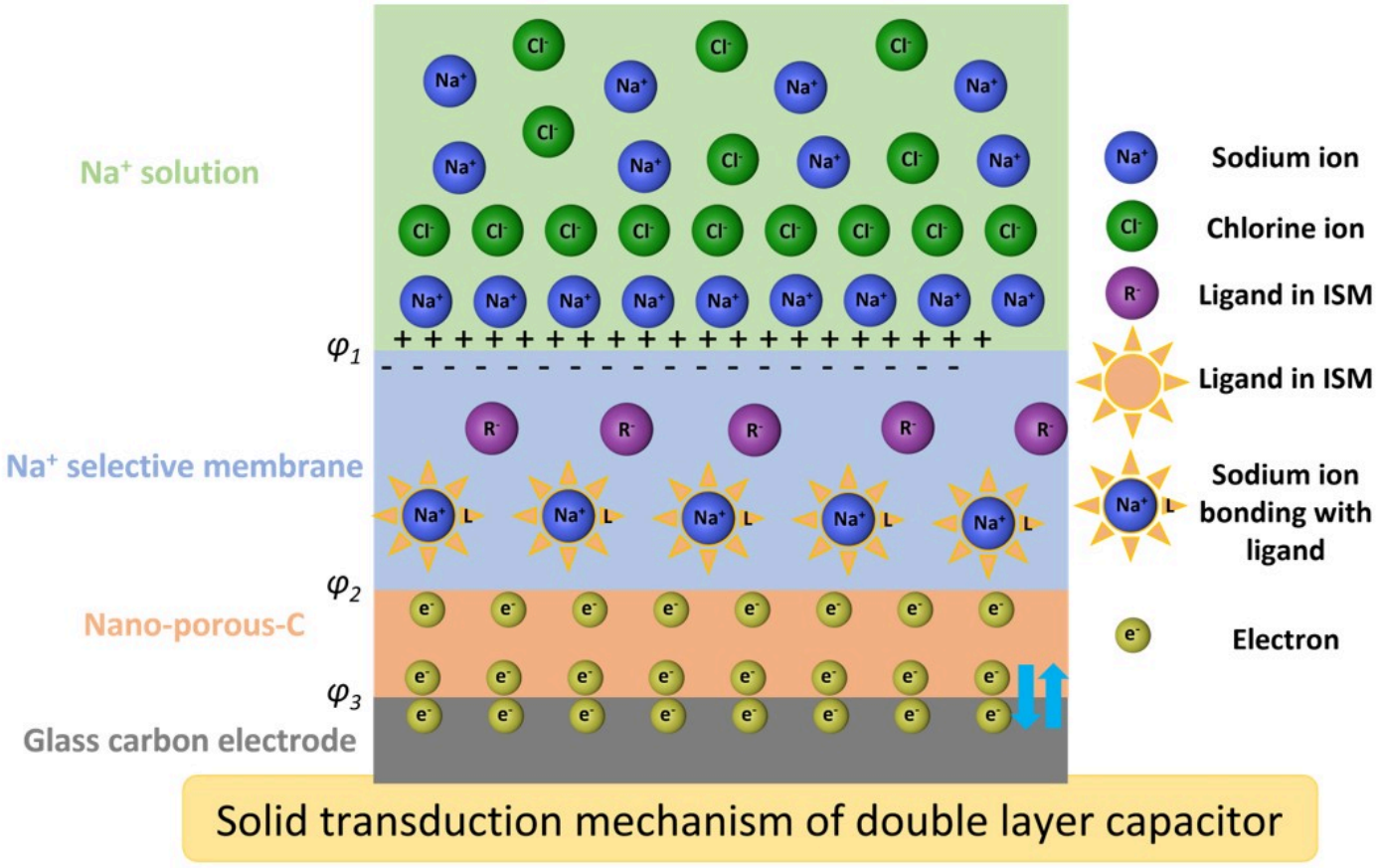


Figure 5

Schematic of the solid transduction mechanism of NPC in SC-ISEs

Supplementary Files

This is a list of supplementary files associated with this preprint. Click to download.

- 260331Supplementary.docx